



# Finding defects in texture using regularity and local orientation

D. Chetverikov<sup>a,\*</sup>, A. Hanbury<sup>b</sup>

<sup>a</sup>*Computer and Automation Research Institute, Kende u.13-17, H-1111, Budapest, Hungary*

<sup>b</sup>*Centre of Mathematical Morphology, 35, rue St-Honoré, 77305 Fontainebleau Cedex, France*

Received 24 January 2001; received in revised form 30 July 2001; accepted 29 August 2001

---

## Abstract

We address basic aspects of detection of structural defects in regular and flow-like patterns (textures). Humans are able to find such defects without prior knowledge of the defect-free pattern. This capability to perceive local disorder has not attracted proper attention in machine vision, despite its obvious relation to various application areas, e.g., industrial texture inspection. Instead, numerous ad hoc techniques have been developed to locate particular sorts of defects for particular tasks. Although useful, these techniques do not help us understand the nature of structural defects, which is the primary goal of our study. In no attempt to compete with the existing dedicated algorithms, we approach texture defects based on two fundamental structural properties, regularity and local orientation (anisotropy). The two properties belong to a hierarchy of structural descriptions, with the former being a higher level one than the latter. Both properties have great perceptual value. In this study, they are assumed to underlie recognition of structural defects. Defects are viewed as inhomogeneities in regularity and orientation fields. Two distinct but conceptually-related approaches are presented. The first one defines structural defects as regions of abruptly falling regularity, the second one as perturbations in the dominant orientation. Both methods are general in the sense that each of them is applicable to a variety of patterns and defects. However, they are better suited to different kinds of patterns. Two tests are presented to assess and compare the two methods. In the first test, diverse textures are processed individually and defects are searched in each pattern. In the second test, classified defects in groups of textiles are considered. Conclusions concerning the scopes of the two approaches are drawn. © 2002 Pattern Recognition Society. Published by Elsevier Science Ltd. All rights reserved.

**Keywords:** Texture analysis; Defect detection; Regularity; Orientation; Mathematical morphology

---

## 1. Introduction

Humans have a surprising capability to easily find imperfections in repetitive spatial structures. This visual mechanism works even when we do not know what the ideal pattern is, and what the possible types of defect are. Just briefly looking at a relatively regular structure containing an imperfection, we can usually tell what is wrong there. This basic property of human vision to readily perceive local

disorder has not received proper attention in computer vision, although it is likely to be related to numerous applications.

One can object that the notion of imperfection is subjective. Human judgement is, as usual, influenced by expectations and prior knowledge. However, this problem is not specific to structural defects. In many detection tasks—for example, edge detection—there is a gradual transition from presence to absence. On the other hand, in ‘obvious’ cases most naive observers agree that the defect is there, even when they cannot identify the structure.

In the related visual inspection tasks [1], trained supervisors are used to determine the ground truth. Defect

---

\* Corresponding author. Tel.: +36-1-2096510; fax: +36-1-1667503.

E-mail address: csetverikov@sztaki.hu (D. Chetverikov).

criteria are set that involve tolerances for structural parameters, such as absence of some elements; deviations in their appearance, size, orientation and layout; presence of undesired objects. These tasks are often referred to as visual *texture inspection*, meaning by texture a non-figurative, repetitive visual structure.

Numerous methods have been designed to solve particular texture inspection tasks: inspection of textile [2,3], wood [4], paper [5] and leather [6], to mention just a few. At the same time, very few attempts have been made to investigate the common background of diverse texture inspection problems. Previous efforts to build a unifying approach include an early categorisation of texture defects [7] and the initial attempt [8]. Song et al. [9] presented a Wigner filter based approach to detect synthetic cracks in random and regular patterns. Defect detection in random colour textures is addressed in Ref. [10]. A survey on defect detection in textures is given in Ref. [11], where more references to previous work, mostly applications, can be found.

It should be emphasised that defect detection in texture and *segmentation* by texture are two different problems. In segmentation [12], an image is partitioned into a set of homogeneous regions, each one being represented by a distinct cluster in the texture feature space. In defect detection, defect-free regions form a cluster, while the outliers, produced by defects, do not.

In some applications, such as textile inspection [3], *classification* of the detected defects may be required. Defects should be categorised into prescribed groups: for example, defects of certain technological origin. Classification assumes detailed knowledge of specific properties and appearance of each particular type of defect. This task-dependent problem is not considered in this paper, as our treatment of the visual phenomenon is intended to be as general as possible.

This study aims at better understanding the nature of structural defects. In particular, we are seeking to express the notion of defect in terms of basic, intelligible visual features. This is in contrast to the most previous studies, which offer efficient but limited-scope techniques to detect specific defects in specific textures. In such studies, a typical industrial approach is often adopted, when many texture features are implemented and tested without any serious attempt to clarify their perceptual meaning.

We do not intend to compete with the existing dedicated algorithms in detecting some particular kind of defects. Instead, we approach the problem of texture defect detection in a more theoretical way, based on two general perceptual criteria: regularity (periodicity) and local orientation (anisotropy). Regularity and anisotropy are two of the *fundamental structural properties* (FSPs) of the visual world [13]. These two features, along with symmetry, self-similarity and other FSPs, underlie basic principles of natural sciences, including fundamental laws of physics and biology. The fundamental properties are intrinsic to the natural and artificial processes that form shapes and patterns.

Appearance of objects and events, the way we perceive and describe them, are strongly influenced by the underlying FSPs whose perceptual value has been demonstrated in many studies.

Regularity and anisotropy belong to a hierarchy of structural descriptions of a pattern. A periodic pattern is always anisotropic, in the sense that it always has one or more characteristic directions defined by its periodicity vectors. Regularity is therefore a higher level description corresponding to a higher level organisation of structure. Selection of regularity and anisotropy is motivated by the dominant role these features play in human texture perception, as studied by Rao and Lohse [14].

Recently, a new type of an orientation-selective neuron has been discovered in the visual cortex of monkeys [15]. Called the grating cell, this neuron responds to a grating of bars of certain orientation, position and periodicity. This discovery also supports the choice of periodicity and orientation for analysis of oriented structures. Kruijzinga and Petkov [16] discuss the possible impact of the grating cell studies on image processing and propose a computational model, which is applied to texture. Earlier, Rao [17] and Bigün et al. [18] proposed filters to compute dominant local orientation in uni-directional (flow-like) patterns. These filters are selective to orientation only; they do not respond to periodicity.

A structural defect is a result of perturbation in the process that generates the pattern. For example, flaws in textile arise because of minor technological disruptions of mechanical or chemical nature. As it develops in time and spreads in space under some constraints, a generating process has its intrinsic anisotropy, symmetry, and, possibly, periodicity. These features are sensitive to perturbations, and it is natural to use them as a general basis for definition and detection of structural defects. We quantify orientation coherence and regularity and apply them to defect detection in textures. Defects are viewed as inhomogeneities in regularity and orientation fields.

Two approaches are presented in this paper, which is structured as follows. The regularity-based algorithm is discussed in Section 2. It searches for *irregularities*—regions where regularity is significantly lower than its dominant value. Regularity features are computed for a set of windows, then defects are identified as outliers in the regularity feature space. The orientation-based method is described in Section 3. This algorithm finds defects as *perturbations in the dominant orientation* or orientation coherence. A morphological top-hat filter is used to emphasise the regions of perturbations. For some less homogeneously oriented textures, however, non-defects also sometimes perturb the orientation or orientation coherence. In this situation, extra morphological filtering has to be performed to exclude non-defects. This is an additional demonstration of the positions of orientation and regularity in the FSP hierarchy—orientation, being lower, requires a more detailed description of its defects.

To demonstrate the generality of the approaches, in Section 4 we first apply them to diverse patterns that contain structural defects as perceived by a naive observer. Then classified defects in textiles are processed in order to test the capability to solve an applied problem with specific ground truth. Finally, conclusions concerning the scopes of the two approaches are drawn.

## 2. The regularity approach

In this section, we discuss the regularity-based approach to detect structural defects. The approach assumes that the basic, defect-free pattern is homogeneous and shows some periodicity. First, regularity features are defined. These features were already introduced in a recent paper [19], so a sketch of the computational definition is only given. In the second part of this section, we present the outlier detection procedure, which finds those points in the regularity feature space that fall far from the cluster formed by the basic, defect-free pattern.

The algorithm described in this section is called StrucDef. It has been developed by the Image and Pattern Analysis (IPAN) group of the Computer and Automation Research Institute, Budapest, Hungary. Online demonstration of StrucDef is available on the Internet at the web site of IPAN:

<http://visual.ipan.sztaki.hu>

Full access to the executable program is provided, including the possibility to set the parameters and run the algorithm on remote user's own data.

Executables of StrucDef and other related programs are available on request from the corresponding author.

### 2.1. The regularity features

The regularity method quantifies pattern regularity by evaluating, in polar co-ordinates, the periodicity of the autocorrelation function. Consider an  $N \times N$  pixel size digital image  $I(m, n)$  and a spacing vector  $(d_x, d_y)$ . Denote by  $\rho_{xy}(d_x, d_y)$  the normalised autocorrelation of  $I(m, n)$ . We obtain  $\rho_{xy} \in [0, 1]$  via the FFT using the well-known relation [20] between the correlation function and the Fourier transform.

The polar representation  $\rho_{pol}(\alpha, d)$  is then computed on a polar grid  $(\alpha_i, d_j)$  by interpolating  $\rho_{xy}(d_x, d_y)$  in non-integer locations. The resulting matrix is denoted by  $\rho_{pol}(i, j)$ . The negated matrix is then used, referred to as the polar *interaction map* [19]

$$M_{pol}(i, j) = 1 - \rho_{pol}(i, j).$$

A row of  $M_{pol}(i, j)$  is called a *contrast function*. A contrast function  $F_i(j)$  shows the variation of contrast with spacing  $d_j$  along direction  $i$  (see Fig. 1). A periodic texture has contrast functions with deep and periodic minima. Our definition of regularity quantifies this property.

For an angle  $i$ , the *directional regularity* is defined as

$$R(i) = [R_{int}(i)R_{pos}(i)]^2,$$

where the  $R_{int}(i)$  and  $R_{pos}(i)$  are the *intensity regularity* and the *position regularity*, respectively.  $R_{pos}(i)$  reflects the regularity (periodicity) of the layout of the elements comprising the pattern, while  $R_{int}(i)$  indicates how regular (stable) the intensity of the elements is. The main steps of the algorithm that computes  $R_{int}(i)$  and  $R_{pos}(i)$  are as follows.

Step 1 applies a filter to remove noisy extrema in  $F(j)$ , then finds the relevant extrema. Step 2 determines the amplitudes of  $F(j)$  by assigning a minimum to each maximum. Then the largest amplitude  $F_{max} - F_{min}$  is selected. Finally, the intensity regularity is defined as

$$R_{int} = 1 - \frac{F_{min}}{F_{max}}.$$

Step 3 finds the positions  $j_1$  and  $j_2$  of the two lowest minima ( $j_1 < j_2$ ). Then the position regularity is defined as the measure of how close  $2j_1$  is to  $j_2$

$$R_{pos} = 1 - \left| 1 - \frac{2j_1}{j_2} \right|.$$

This means that  $j_1$  is the first,  $j_2$  is the second period. The variant that  $j_2$  is the third period is also considered (see Fig. 2).

The two *regularity features* are then defined as follows. Denote by  $T_k$  the sequence of the local maxima values of  $R(i)$ . (Positions of  $T_k$  within  $R(i)$  do not matter.) To select the relevant maxima, we threshold them at  $T_{thr} = 0.15$ . Two features are then calculated in the thresholded sequence: the largest value  $M_R$  and the mean  $\mu_R$ . (More features can be defined for other tasks [19].)  $0 \leq \mu_R \leq M_R \leq 1$ , with 0 indicating a random, 1 a highly regular pattern.  $M_R \geq 0.25$  means visually perceived periodicity.

### 2.2. Outlier detection

The two regularity features are computed for a set of windows covering the image. Most of the windows contain the basic, defect-free pattern, while some windows may contain defects. In the feature space, defect-free windows produce a cluster grouped around a 'typical' point. Defective windows result in outliers whose distances from this point exceed the radius of the cluster. 'Positive' outliers, that is, areas of unusually high regularity may also exist. Since in most applications such regions are not considered to be defects, we discard them in a post-processing step of the algorithm.

The principle of the algorithm is illustrated in Fig. 3. Its idea comes from the theory of robust regression and outlier detection [21]. Let the regularity feature vectors of the windows be  $\mathbf{p}_i$ . The vectors are represented by points in the feature space; a majority of them forms a cluster. First, we find the *central point*  $\mathbf{p}_c$  of the cluster as the point whose median distance from all other points is minimal:

$$d_{med}(c) < d_{med}(i) \quad \text{for all } i \neq c, \quad (1)$$

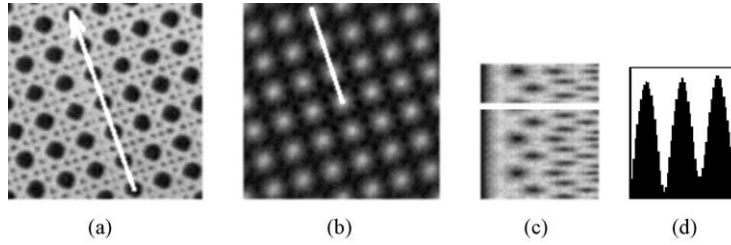


Fig. 1. Computing contrast function (a) a pattern and a direction within the pattern, (b) autocorrelation function, (c) polar interaction map and (d) contrast function for the direction.

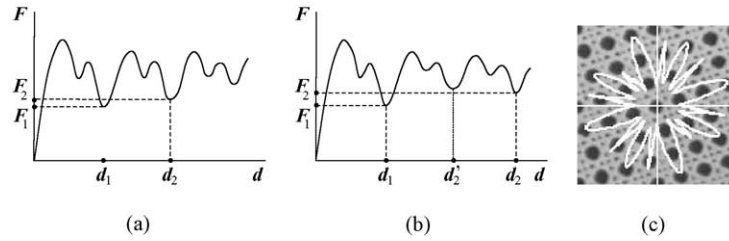


Fig. 2. Computing directional regularity  $R(i)$ , (a)  $j_2$  is the second period, (b)  $j_2$  is the third period and (c) polar plot of  $R(i)$  overlaid on the pattern.

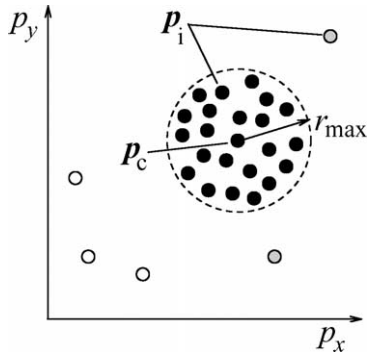


Fig. 3. Principle of outlier detection. Empty and grey circles are outliers. The grey ones are discarded during the post-processing.

where

$$d_{med}(i) = \text{median}_{j \neq i} \|\mathbf{p}_i - \mathbf{p}_j\|.$$

$\mathbf{p}_c$  is the innermost point of the cluster. We call the distance between a point  $\mathbf{p}_i$  and the centre  $\mathbf{p}_c$  the *radius*  $r_i$  of  $\mathbf{p}_i$

$$r_i = \|\mathbf{p}_i - \mathbf{p}_c\| \quad (2)$$

and denote by  $r_{mean}$  the mean radius of the cluster.

A point  $\mathbf{p}_k$  is then selected as an *outlier* if its radius exceeds a threshold  $r_{max}$ :  $r_k > r_{max}$ . (Another, fixed threshold discards minor, irrelevant variations.) In our tests the value of  $r_{max}$  is set in two different ways. When no ground truth is available for prior learning (test 1), the threshold is set as  $r_{max} = Kr_{mean}$ , where  $K$  is a parameter whose typical range

of values is 2–4. When the ground truth is available (test 2),  $r_{max}$  is learned from the distribution of the radius values obtained for the reference defect-free patterns.

Alternatively, one can use the robust standard deviation estimate [21]:  $\hat{\sigma} = 1.4826d_{med}(c)$ , and detect outliers as  $r_k > K\hat{\sigma}$ . We have experienced that relating the threshold to  $r_{mean}$  rather than  $d_{med}(c)$  gives somewhat better result.

‘Negative’ outliers of low regularity are only accepted as defects. In the post-processing step, an outlier  $\mathbf{p}_k$  is discarded if  $p_{kx} > p_{cx}$  or  $p_{ky} > p_{cy}$  (see Fig. 3).

Besides the thresholding factor  $K$ , the regularity-based algorithm, StrucDef, has only two parameters: the detector window size  $W$  and the window slide step  $S$ .  $W$  is the critical parameter to be selected carefully. The window must span several periods of the structure. At the same time, it should be as close to the expected defect width as possible.  $S$  is much less critical. Basically, one has to balance between more reliable detection and higher processing speed.

The small number of parameters reflects the generality of the regularity approach. Any defect is viewed as just a significant decrease in regularity.  $W$  and  $K$  are only needed to tune the algorithm to the period of structure and the spread of the cluster in the feature space. The advantages and drawbacks of the generality will be discussed in Section 5.

### 3. The orientation approach

In this approach, defects are identified due to perturbations in the dominant orientation or orientation coherence

of the images. The dominant orientation is calculated using an algorithm developed by Rao [17]. This algorithm produces two images for each input image, the first containing the dominant orientations in each neighbourhood, and the second containing the orientation coherence. As we are not dealing with vector fields, but axial data, the values in the orientation image are between  $0^\circ$  and  $180^\circ$ .

Contrary to regularity, the orientation algorithm is adapted to the input data not only in terms of its parameters, but also in terms of its control structure. Based on the dominant orientation—the engine of the approach—two different procedures are used for the two different datasets considered in the experimental study. This is done in an attempt to adapt the orientation algorithm to multidirectional structures, such as tiles. The original approach by Rao [17] is only applicable to the unidirectional, flow-like patterns.

The approach described in this section has been developed by the Centre of Mathematical Morphology, Fontainebleau, France. As much use is made of mathematical morphology in this section, we begin with a brief recapitulation of these operators.

### 3.1. Mathematical morphology

Mathematical morphology [22] is a theory and technique for the analysis of spatial structures, which has been applied very successfully to image analysis. A good practical introduction is given by Soille [23]. We assume that the reader is familiar with the basic operations of greyscale morphology, such as erosion, dilation, opening and closing. A few more sophisticated operators used in this article are defined below. We restrict ourselves to the specific case of a two-dimensional digital image  $I$  defined on a square grid  $Z \subset \mathcal{Z}^2$  such that  $I: Z \rightarrow \{0, 1, 2, \dots, t_{\max}\}$ , where  $t_{\max}$  is the maximum value of the data type used to store the image. For eight-bit greyscale images,  $t_{\max} = 255$ ; and for binary images,  $t_{\max} = 1$ .

The operators make use of a structuring element  $B$ , which is a set of points with a specified origin. The notation  $B_x$  represents a structuring element which has been translated so that its origin is at position  $x$  in  $Z$ . As the square structuring element is used extensively, the notation  $S_i$  will be used to indicate a square structuring element of size  $i$ , which has sides of length  $2i + 1$ . So  $S_1$  is a  $3 \times 3$  square,  $S_2$  is a  $5 \times 5$  square, etc.

The *erosion* of  $I$  by structuring element  $B$  is denoted by  $\varepsilon_B I(x)$ ; the *dilation* is denoted by  $\delta_B I(x)$ . An alternative notation for the erosion is  $I \ominus B$ , for the dilation  $I \oplus B$ . The *opening* is defined as  $\gamma_B I = (I \ominus B) \oplus B$ , the *closing* as  $\phi_B I = (I \oplus B) \ominus B$ .

The *top-hats* are used to locate structures in the image which are smaller than the structuring element. Two top-hats are defined, the white top-hat is the difference between  $I$  and its opening

$$WTH_B(I) = I - \gamma_B I \quad (3)$$

and the black top-hat is the difference between the closing of  $I$  and  $I$

$$BTH_B(I) = \phi_B I - I. \quad (4)$$

A *geodesic dilation* involves two images: a marker image  $I$  and a mask image  $g$ , both defined on the same domain  $Z$ . The geodesic dilation of  $I$  with respect to the mask image  $g$  is defined as

$$I \oplus_g B = (I \oplus B) \wedge g$$

or the point-wise minimum between the dilation of  $I$  and  $g$ .

The *geodesic reconstruction*  $R_g$  is defined as the iteration until convergence of geodesic dilations of  $I$  with respect to  $g$  by the elementary structuring element  $S_1$ . If we use the notation  $\delta_g^{(n)}(I)$  to indicate  $n$  iterations of a geodesic dilation of  $I$  with respect to  $g$  using  $S_1$ , then the geodesic reconstruction of  $I$  with respect to  $g$  is

$$R_g(I) = \delta_g^{(m)}(I) \quad (5)$$

such that  $\delta_g^{(m)}(I) = \delta_g^{(m+1)}(I)$ . For binary images, this has the effect of completely reconstructing the connected components in the mask image  $g$  which have at least one non-zero pixel in common with the marker image  $I$ .

In a binary image, an *area opening*  $\gamma_\lambda$  removes all the connected components with an area less than a certain threshold  $\lambda$ . It can be shown that this is equivalent to the union of all openings with connected structuring elements whose areas are equal to  $\lambda$

$$\gamma_\lambda = \bigvee_i \{\gamma_{B_i} \mid B_i \text{ is connected and Area}(B_i) = \lambda\}. \quad (6)$$

### 3.2. The Rao algorithm

This algorithm computes the dominant orientation and angular coherence. It has the following steps [17]:

- The greyscale image is smoothed by a Gaussian kernel with deviation  $\sigma_1$ .
- Horizontal and vertical gradients are calculated on the smoothed image.
- At each pixel  $(i, j)$ , a magnitude  $R_{ij}$  and angle  $\theta_{ij}$  (between  $0^\circ$  and  $360^\circ$ ) are calculated from the gradient images.
- A square neighbourhood  $W$  of side  $\sigma_2$  is then moved over the image in steps of  $\Delta$  pixels. At each window position  $(x, y)$ , the dominant local orientation  $\hat{\theta}_{xy}$  (between  $0^\circ$  and  $180^\circ$ ) and angular coherence  $\kappa_{xy}$  (between 0 and 1) are calculated: d

$$\hat{\theta}_{xy} = \frac{1}{2} \arctan \frac{\sum_{(i,j) \in W} R_{ij}^2 \sin 2\theta_{ij}}{\sum_{(i,j) \in W} R_{ij}^2 \cos 2\theta_{ij}} \quad (7)$$

and

$$\kappa_{xy} = \frac{\sum_{(i,j) \in W} |R_{ij} \cos(\hat{\theta}_{xy} - \theta_{ij})|}{\sum_{(i,j) \in W} R_{ij}}. \quad (8)$$

The values of the parameters  $\sigma_1$ ,  $\sigma_2$  and  $\Delta$  are set depending on the type of the input data, as discussed in Section 4. The values of  $\hat{\theta}_{xy}$  and  $\kappa_{xy}$  are placed into an orientation image  $\hat{\theta}_{ij}$  and coherence image  $\bar{\kappa}_{ij}$ , in which each pixel represents the value calculated in a neighbourhood. In symbolic form,  $\hat{\theta}_{ij} = \hat{\theta}_{(i \times \Delta)(j \times \Delta)}$  and  $\bar{\kappa}_{ij} = \kappa_{(i \times \Delta)(j \times \Delta)}$ .

### 3.3. Defect detection in the Brodatz images

Two types of test data are considered in our experimental study. As already mentioned, the two datasets have different characters, requiring different ways of locating singularities in orientation and its coherence. The Brodatz images [24] are shown in Section 4.1, the textile images of the TILDA database [25] in Section 4.2.

For detection of defects on the Brodatz images, it is sufficient to use only the orientation image, as these defects are small blob-like regions characterised by having a different orientation to that of the surrounding region (a singularity in the orientation field). These small regions can be emphasised by using a morphological top-hat filter adapted for use on images encoding angular information [26]. This top-hat is defined for each pixel  $x$  on an angular image  $a$  as

$$(\text{top-hat})(x) = -\sup\{\inf[-(a(x) \div a(y)), y \in B_i], i \in I\}, \quad (9)$$

where  $B$  is a structuring element and  $\{B_i, i \in I\}$  is the family of such structuring elements which contain point  $x$ . For blob-like structures,  $B$  should be chosen as a square with an area larger than the defect it is being used to emphasise. The operator  $\div$  is defined as

$$a \div a' = \begin{cases} |a - a'| & \text{if } |a - a'| \leq 180^\circ, \\ 360^\circ - |a - a'| & \text{if } |a - a'| \geq 180^\circ. \end{cases} \quad (10)$$

The resulting top-hat image can then be thresholded to locate the position of the defect.

### 3.4. Defect detection on the textile images

As we are using a mathematical morphology approach to the detection of defects, it is necessary to give a clear description of the characteristics of the defects to be located. For the textile images, finding regions of anomalous orientation is not sufficient, as many of the textiles have highly variable orientation fields. We therefore begin by considering the orientation coherence.

Sample textile images of the TILDA database [25] are shown in Section 4.2. For textiles having a low global orientation coherence, regions of high coherence are taken as candidates for defects, and vice versa for textiles having high global coherence. However, using only this information leads to a large number of non-defect regions being falsely detected as defects, so additional characteristics are added. The general descriptions of the two types of defects

that this approach has been tuned to detect are:

- A contiguous region of high/low coherence associated with a bright or dark blob on the intensity image.
- A large contiguous region of high/low coherence having an average orientation significantly different to the global average orientation, or having a high orientation variance.

We have heuristically defined a high coherence as being 0.9 and above, and a low coherence as being below 0.9. The procedures for the automatic location of these two types of defect are described here.

The treatment of the coherence images for both types of defect model is the same:

- (1) Initially, depending on the global coherence of the textile, we extract the regions of high or low coherence. This is done by thresholding the coherence image  $\bar{\kappa}$  (Eq. (8)) to produce a binary image  $\bar{\kappa}^b$ , where for high coherence regions

$$\bar{\kappa}_{ij}^b = \begin{cases} 1 & \text{if } \bar{\kappa}_{ij} \geq 0.9, \\ 0 & \text{if } \bar{\kappa}_{ij} < 0.9 \end{cases}$$

and vice versa for low coherence regions.

- (2) The binary image  $\bar{\kappa}^b$  is closed by  $S_3$

$$\bar{\kappa}^{bm} = \phi_{S_3} \bar{\kappa}^b$$

to connect nearby regions which most likely are associated with the same defect.

An example of this processing for high coherence defects is shown in Fig. 4, in which (b) is the coherence image of (a), (c) is the thresholding of the coherence image, and (d) shows the result of the closing operator on (c).

#### 3.4.1. Bright or dark spot defects

Here, we find high/low coherence regions associated with bright or dark spots on the greyscale image  $I$ . The procedure for extracting the bright spots is explained, with the only change needed to extract the dark spots being in the threshold in step 2.

- (1) This step corrects the uneven illumination by using a white top-hat (3) with a large structuring element

$$I^l = WTH_{S_{30}}(I).$$

- (2) A simple automatic thresholding of  $I^l$  is performed. The limit  $t$  is chosen as the highest greylevel with more than 200 pixels in  $I^l$ .

$$I_{ij}^{lb} = \begin{cases} 1 & \text{if } I_{ij}^l \geq t, \\ 0 & \text{if } I_{ij}^l < t. \end{cases}$$

The value of  $t$  is not critical. It should be low enough to extract a significant number of pixels from a bright blob. The next step serves to improve the results of this threshold.

- (3)  $I^{lb}$  is dilated by  $S_3$  to join up nearby pixels which most likely belong to the same bright blob, after which

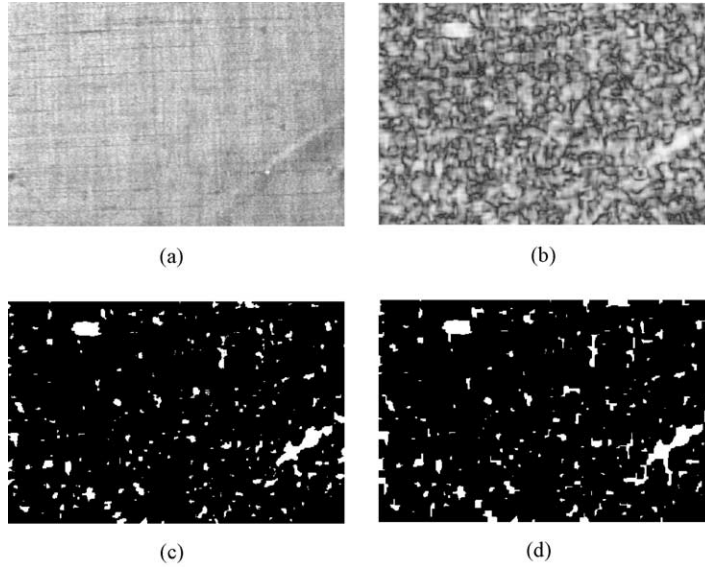


Fig. 4. The processing of the coherence image (a) original image, (b) coherence image, (c) binary coherence image and (d) binary coherence image after morphological processing.

connected components with areas of less than 10 pixels are removed.

$$I^{lbm} = \gamma_{10}(I^{lb} \oplus S_3).$$

- (4) The final step is to find regions in the binary coherence image  $\tilde{\kappa}^{bm}$  which are associated with a bright blob. For this,  $I^{lbm}$  is dilated by  $S_8$  to ensure overlap, and then the mask image  $\tilde{\kappa}^{bm}$  is reconstructed using  $(I^{lbm} \oplus S_8)$  as marker image, or

$$\tilde{\kappa}^{\text{defect}} = R_{\tilde{\kappa}^{bm}}(I^{lbm} \oplus S_8),$$

where  $\tilde{\kappa}^{\text{defect}}$  is the binary image containing only the bright spot defects (see Section 3.1).

Fig. 5 shows an example of this sequence of treatment, where (a) is the threshold on the illumination corrected version of Fig. 4a, (b) is the result of the morphological treatment, (c) is the reconstruction of Fig. 4d from (b), and (d) shows the defect superimposed on the illumination corrected image.

#### 3.4.2. Anomalous orientation defects

Here, we consider the large regions of high/low coherence, examine their angular statistics, and make a decision as to whether the region is a defect or not.

- (1) An area opening (Eq. (6)) of size 500 pixels is applied to  $\tilde{\kappa}^{bm}$

$$\tilde{\kappa}^{bma} = \gamma_{500}(\tilde{\kappa}^{bm}).$$

- (2) Each remaining connected component (region) in image  $\tilde{\kappa}^{bma}$  is notated as  $M_l$  with index  $l$ . The angular mean  $\mu_l$  and sample circular variance  $V_l$  [27] of each  $M_l$  are

calculated using the values in the orientation image  $\bar{\theta}$ , where

$$\mu_l = \begin{cases} \arctan \frac{S_l}{C_l} & \text{if } S_l > 0, C_l > 0, \\ \arctan \frac{S_l}{C_l} + 180^\circ & \text{if } C_l < 0, \\ \arctan \frac{S_l}{C_l} + 360^\circ & \text{if } S_l < 0, C_l > 0, \end{cases}$$

where

$$C_l = \sum_{\bar{\theta}_{ij} \in M_l} \cos \bar{\theta}_{ij}, \quad S_l = \sum_{\bar{\theta}_{ij} \in M_l} \sin \bar{\theta}_{ij},$$

$$R_l^2 = C_l^2 + S_l^2$$

and

$$V_l = 1 - \frac{R_l}{\text{Area}(M_l)}.$$

The area is measured in pixels. The circular variance is in the range [0, 1]. For highly clustered data, it is close to 0, and it increases for more widely spread data.

- (3) The global angular mean  $\bar{\mu}$  of the image  $\bar{\theta}$  is calculated.  
 (4) A region  $M_l$  is retained as a defect if the following criteria are met:

$$[\mu_l \div \bar{\mu}] > 20^\circ \quad \text{and} \quad [\mu_l \div (\bar{\mu} + 90^\circ)] > 20^\circ$$

or

$$V_l > \frac{1}{2}.$$

In other words, regions are considered to be defects if they are oblique with respect to the dominant orientations, or if they have high angular variance. Note that the sum  $(\bar{\mu} + 90^\circ)$  must be taken modulus  $180^\circ$ .

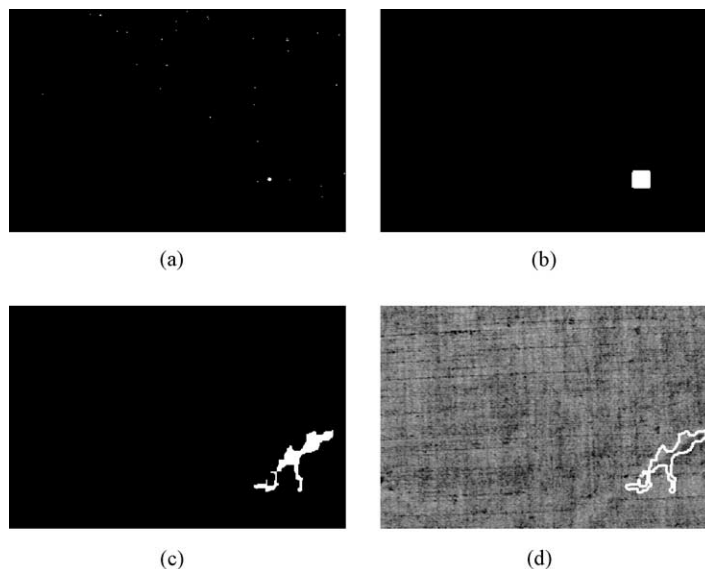


Fig. 5. The processing to extract areas of high coherence associated with bright blobs (a) thresholding of Fig. 4a, (b) result of the morphological processing of (a), (c) the morphological reconstruction of Fig. 4d from (b) and (d) the defect superimposed on the image.

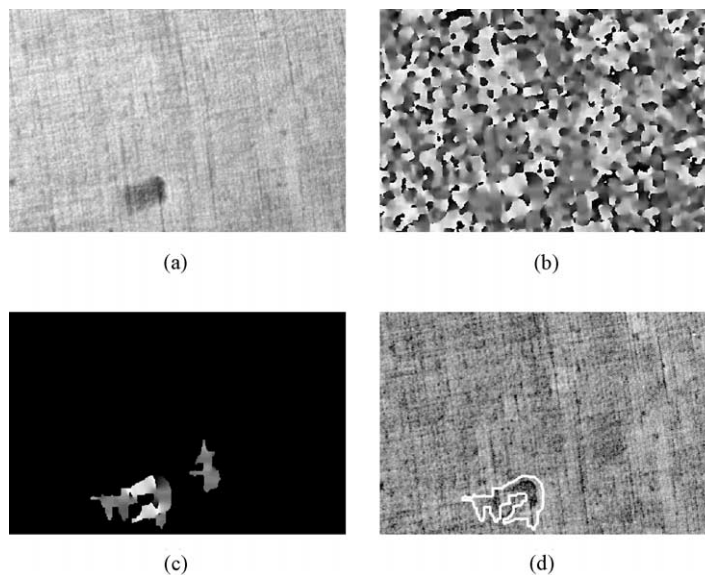


Fig. 6. The processing to extract areas of high coherence and anomalous orientation (a) original image, (b) orientation image, (c) the orientation image masked by the large areas of high coherence and (d) the defect superimposed on the image.

Fig. 6 presents an example of this sequence of treatment, where (b) is the orientation image of (a) and (c) is the orientation image masked by the large areas of high coherence. In (c), the region on the right has an angular mean of  $90^\circ$  and sample circular variance of 0.06, and the region on the left has an angular mean of  $107^\circ$  and sample circular variance of 0.71. Only the region on the left is considered to be a defect as it has a high circular variance. This defect

superimposed on the illumination corrected initial image is shown in Fig. 6d.

#### 4. Tests

Two different tests were carried out to assess the efficiency of the approach. In both tests, the regularity and the



orientation approaches were found to be best applicable to different patterns, with a certain overlap between the scopes, as discussed later in this section. For this reason, the pictorial, qualitative results obtained by the two algorithms are presented separately. When ground truth is available (test 2), quantitative results are obtained and presented jointly for better comparison of the scopes of the approaches.

#### 4.1. Test 1: Brodatz patterns

In this test, nine  $256 \times 256$  pixel size patterns from the album [24] and an additional ‘home-brewed’ pattern (d000) were used. The images have been normalised to span the standard intensity range. The textures contain more or less obvious imperfections. No ground truth was available in this case. Qualitative pictorial results were obtained, to be assessed visually. First, we present the results of the regularity-based algorithm StrucDef. Then the results of the orientation approach are shown.

##### 4.1.1. Regularity

For each pattern, the optimal value of the threshold parameter  $K$  was selected manually. The window size was set so as to include at least two periods of the pattern. Typically, this size was at least  $40 \times 40$  pixels and a few hundred overlapping windows were processed in 20–50 s.

The regularity results are summarised in Fig. 7. In each pair, the left image (‘det’) shows the areas that were found to be defective, while the right image (‘imp’) displays the corresponding intensity-coded *distance map*. A distance map shows distances from the central point of cluster—the radii of Eq. (2). The distance is a measure of imperfection. Brighter points indicate more distant outliers that are more likely to be defects. The distance maps have been enhanced for better visibility.

Linear as well as blob-like defects have been successfully detected in all ten images. Patterns d022, d079 and d103 deserve some comments. Image d079 can be interpreted as having a blob-like and/or a linear defect. Both defects can be observed in the distance map. Patterns d022 and d103 can be interpreted as having multiple defects. The most distinct of them are only shown.

##### 4.1.2. Orientation

The orientation images for the Brodatz textures were calculated using  $\sigma_1 = 1.75$ ,  $\Delta = 2$  and  $\sigma_2 = 16$ , except for patterns d052 and d079, where  $\sigma_2 = 32$  was used. The thresholds on the top-hat images were set manually. The orientation results are summarised in Fig. 8. In each pair, the left image (‘det’) shows the areas that were found to be defective, while the right image (‘tph’) displays the associated top-hat computed by Eq. (9).

Typically, the orientation and coherence images were calculated (using non-optimised routine) in about 1–2 min. The execution time for the top-hat filter depends on the size

chosen, and ranges from 5 s for a square structuring element  $S_1$  to 8 min for  $S_7$ .

The orientation filter is selective to six of the ten Brodatz defects. Most of the Brodatz textures considered are multi-directional, which is a disadvantage for the orientation approach. However, the method is still applicable, except for the four images where the local orientation of the defect-free pattern varies very strongly: textures d003, d022, d036 and d103 of Fig. 7.

#### 4.2. Test 2: TILDA textiles

In the second test, we processed sample images from the TILDA Textile Texture Database [3,25]. Textile defect detection is a traditional industrial application of image processing; two recent studies are Refs. [28,29]. At this point, we have to emphasise again that our goal is not to compete with highly dedicated, limited-scope algorithms aimed at detection of particular defects in particular (e.g., textile) textures. In addition, Ref. [28] presents just a few examples of defect (flaw) detection; no statistical evaluation is given. Study [29] uses banks of Gabor filters optimised to detect five types of flaws in certain woven textiles. Successful detection of flaws in 25 test images is reported; no further quantitative results are provided.

Contrary to our test images (Brodatz, TILDA), test images used in most industrial case studies are not publicly available. This is another reason why no comparison with dedicated algorithms is done in our experimental study.

TILDA has been created by the working group Texture Analysis of the Deutsche Forschungsgemeinschaft, Germany. The database is distributed on 2 CD-ROMs by the University of Freiburg. Textile samples are grouped as defect-free or having a certain type of defect. For each defect type, defect-free samples are provided. The database includes eight categories of textiles, each of them having seven defect classes and one defect-free class. Since each of the classes is represented by 50 images, the database contains the total of 3200 arbitrarily rotated, greyscale textile images of  $768 \times 512$  pixel size. (We resize them by a factor of 0.5, then normalise the grey levels to the standard range.)

Some of the textile images of TILDA are not textures, but figurative patterns containing relatively small number of large-size, distinct shapes. Imperfections in such images are perceived as shape, rather than texture, defects. For this reason, these images were not included in our tests.

The ground truth in TILDA is limited to an indication that a textile pattern is either defect-free or defective, that is, contains a single defect of the type encoded in the name of the image file. No information concerning the position and size of the defect is available, making the automatic assessment of detection results impossible. Given the huge amount of image data and the necessity to visually assess each result separately, we had to reduce the number of images processed.

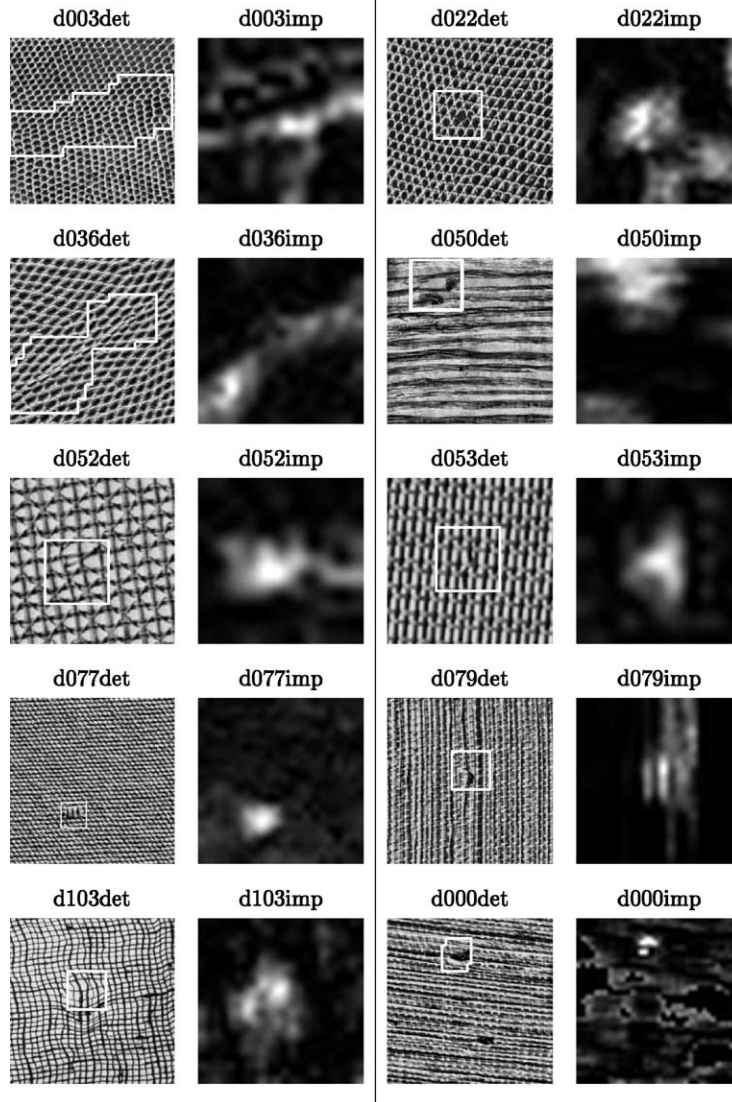


Fig. 7. Test 1. Brodatz images. Results of the regularity approach.

Three groups of textiles, c1, c2, and c3, were considered. (Group c4 is purely figurative.) Each group splits into two categories. Each category included four defect classes e1–e4 and a defect-free class e0. Every class had five images. Altogether,  $3 \times 2 \times 5 \times 5 = 150$  images were processed, including 120 defect images and 30 defect-free images.

Sample pictorial results are shown below. A quantitative summary of the second test is given in Section 4.3.

#### 4.2.1. Regularity

In test 2, StrucDef selects the radius threshold  $r_{max}$  automatically by learning from defect-free patterns. Fig. 9 displays sample detection results for those defect classes whose detection with StrucDef was judged to be possible.

Fig. 10 shows the uncertain cases, when the success was only partial; the limitations will be discussed in Section 4.3.

#### 4.2.2. Orientation

Depending on textile, the regions that are considered to be defects are either characterised by having high orientation coherence (c1r1, c1r3, c2r2 and c2r3) or low orientation coherence (c3r3). The parameters used for the calculation of the orientation (7) and coherence (8) images were  $\sigma_1 = 4.75$ ,  $\Delta = 2$  and  $\sigma_2 = 16$  in all cases.

Fig. 11 displays sample detection results for those defect classes whose detection was judged to be possible. Fig. 12 shows the uncertain cases, when the success was only partial; the limitations will be discussed below.

Table 1  
Detection results for TILDA images. Textile group c1

	r1e0	r1e1	r1e2	r1e3	r1e4	r3e0	r3e1	r3e2	r3e3	r3e4
Regularity	—	—	—	—	—	0	5:0	3:2	5:1	—
Orientation	0	5:0	5:0	5:1	4:0	1	5:1	5:0	5:1	4:0

Table 2  
Detection results for TILDA images. Textile group c2

	r2e0	r2e1	r2e2	r2e3	r2e4	r3e0	r3e1	r3e2	r3e3	r3e4
Regularity	0	5:1	5:1	4:0	3:0	3	4:1	5:2	3:2	5:1
Orientation	0	5:0	3:0	—	4:0	0	—	—	—	5:0

Table 3  
Detection results for TILDA images. Textile group c3

	r1e0	r1e1	r1e2	r1e3	r1e4	r3e0	r3e1	r3e2	r3e3	r3e4
Regularity	1	—	5:0	—	5:0	1	—	5:0	5:0	5:0
Orientation	—	—	—	—	—	0	4:0	—	3:0	4:0

#### 4.3. Discussion

Tables 1–3 present the quantitative results of test 2 for three groups of textiles, c1, c2, and c3. For every defect-free class e0, the tables give the total number of regions  $N_{err}$  which were erroneously indicated as defects. For a defective class, the total number of the correct detections  $N_{corr}$  versus the total number of misdetections  $N_{false}$  (false positives) is given as  $N_{corr}:N_{false}$ ; the best possible result is therefore 5:0. In a somewhat arbitrary way, detection of a particular defect class is considered possible if  $N_{err} \leq 3$ ,  $N_{corr} \geq 4$  and  $N_{false} \leq 2$ . When  $N_{corr} = 3$ , detection is called less reliable (uncertain case); if  $N_{corr} \leq 2$ , unsuccessful (failure). In the latter case, no numerical result is given, which is indicated by ‘—’.

Let us now assess the performances of the two approaches and discuss their limitations. Sample images of the textiles and defects mentioned in the discussion are shown in Figs. 9–12.

Category c1r1 (Table 1) is composed of low-regularity patterns with relatively distinct directionality. In terms of the regularity features introduced in Section 2.1, this means that in many defect-free regions  $M_R < 0.25$ , which renders StrucDef inapplicable: there is simply no room for significant decrease in regularity. (In addition, variation of the defect-free pattern is considerable.) By contrast, the orientation approach works efficiently, partially because it uses intensity information (light or dark blobs) to assist the detection.

Although the category c1r3 textiles look similar to c1r1, the regularity of most images of c1r3 is higher ( $M_R \geq 0.35$ ). Here, only one of the defects (c1r3e4, Fig. 11) was found

hard to detect. The likely reasons are the small width of this linear defect and/or the lower regularity of the c1r3e4 images. (Each defect class was photographed under different conditions, which might influence the computed regularity.) Here again, the orientation approach works well.

Performance of the regularity approach is usually better for more periodic patterns. The grid-like textiles of group c2r2 (Table 2) are suitable for reliable defect detection, with the exception of defect c2r2e4 (Fig. 10), which is again a narrow linear defect. The orientation approach fails for the hardly visible defect c2r2e3 (Fig. 9); this defect does not cause significant perturbation in orientation.

Category c2r3 is a woven textile with high orientation variation within the images. This renders the orientation approach inapplicable. In addition, some of the defects are difficult to perceive because they look like ‘natural’ pattern variations. However, when the defect is a distinct line (c2r3e4, Fig. 11), it can be reliably detected based on orientation. The regularity approach performs better, although  $N_{err}$  is relatively large because of the high tolerable variation.

The last group of textiles, c3 (Table 3), contains highly periodic textures. This group is especially interesting, since the results illuminate the differences between the two approaches considered. Usually, high periodicity is preferable for the regularity approach and is of no particular value for the orientation approach. The latter prefers unidirectional patterns as well as defects that clearly disturb the local orientation, such as c3r3e4 shown in Fig. 11. On the other hand, defect class c3r3e2 (Fig. 9) cannot be detected because the orientation of local intensity changes is only used: the magnitude is not (see Eq. (7)).

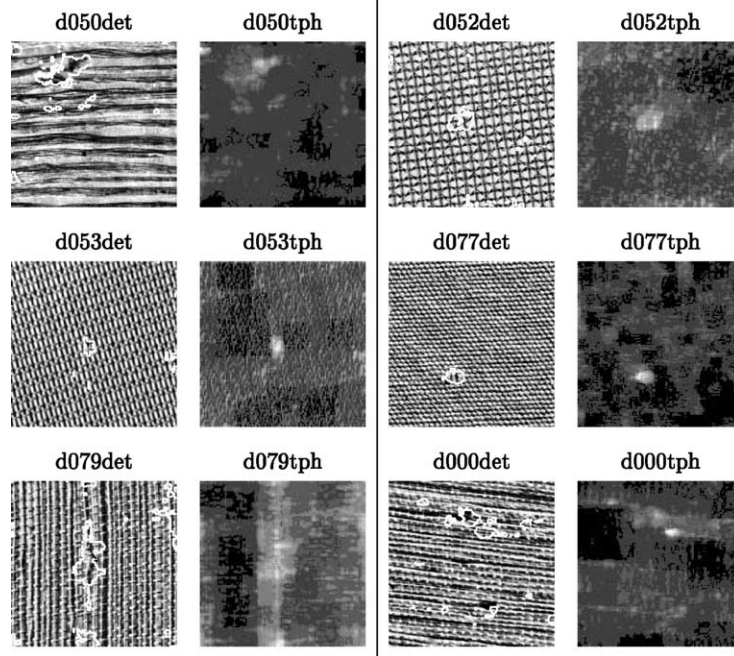


Fig. 8. Test 1. Brodatz images. Results of the orientation approach.

Table 4  
Summary of detection results

	Brodatz images			TILDA classes		
	Success	Failure	Uncertain	Success	Failure	Uncertain
Regularity	10	0	0	13	8	3
Orientation	6	4	0	13	9	2

The multidirectional patterns of category c3r1 (Fig. 9) do not lend themselves to the current version of orientation-based approach. The multidirectionality poses no problem to the regularity approach. However, similarly to the orientation approach, StrucDef cannot detect the pointwise defect c3r1e1 and the very narrow defect c3r1e3, which are shown in Fig. 13. The reason is that the small width of these defects conflicts with the large window needed by StrucDef in order to span at least two periods of the pattern: otherwise, periodicity cannot be observed. The impact of a tiny defect in a large window is negligible.

## 5. Conclusion

Table 4 summarises the quantitative results of the two tests. The regularity approach was more successful in detecting defects in the 10 Brodatz images. For the TILDA dataset comprising 24 defect classes (120 defect images), the overall result is more balanced, as regularity was found

inapplicable to eight classes, compared to nine classes in case of orientation. For the successfully processed classes, the overall indicator  $\sum N_{corr} : \sum N_{false}$  is 63 : 7 for regularity and 60 : 3 for orientation. Orientation seems to yield less true positives and less false positives, which might result from more conservative setting of the detection threshold. Also, recall that the orientation approach uses additional cues to discard non-defective regions, while the regularity approach applies no other features to confine the selection.

For a systematic comparison of the two approaches, more data are needed. Also, the reliability of detection should be taken into account in some form, for example, by comparing response to a defect to the maximal response to a defect-free region. Figs. 7(imp) and 8 (tph) show that separation of defect from basic pattern varies substantially.

Some general conclusions can nevertheless be made based on our current experience of using the two fundamental structural features for texture defect detection. Most importantly, we believe that the two fundamental structural features, regularity and local anisotropy (orientation) can provide a framework for a reasonably general approach to

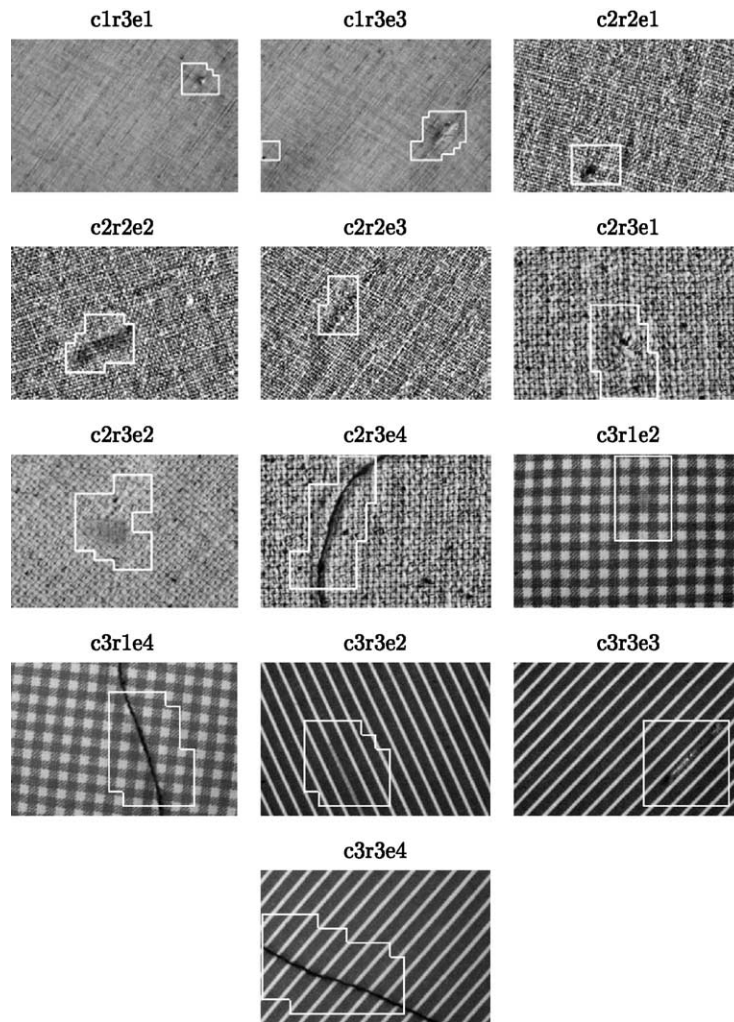


Fig. 9. Test 2. TILDA images. Sample results of the regularity approach. Cases when detection is possible.

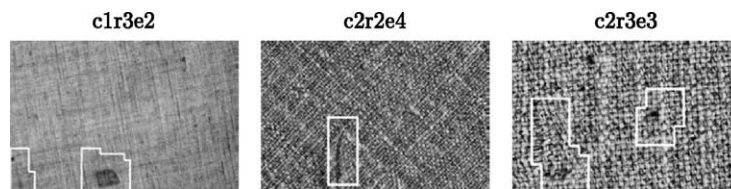


Fig. 10. Test 2. TILDA images. Sample results of the regularity approach. Uncertain cases.

detection of structural imperfections. Since the two methods have different scopes, it seems advantageous to combine them.

In particular, the theoretical attractiveness of the regularity approach lies in its coherent, conceptually uniform treatment of defects in regular structures. As discussed in Section 2, the algorithm has only two basic parameters to

be set, the window size and a defect thresholding parameter. A practical drawback of this generality is that there is no way to tune the algorithm to a particular appearance or geometry of a defect: a defect is just a region where regularity falls. Another essential limitation is that the approach is applicable to neither structures having low regularity  $M_R < 0.25$  (for example, random textures), nor defects that

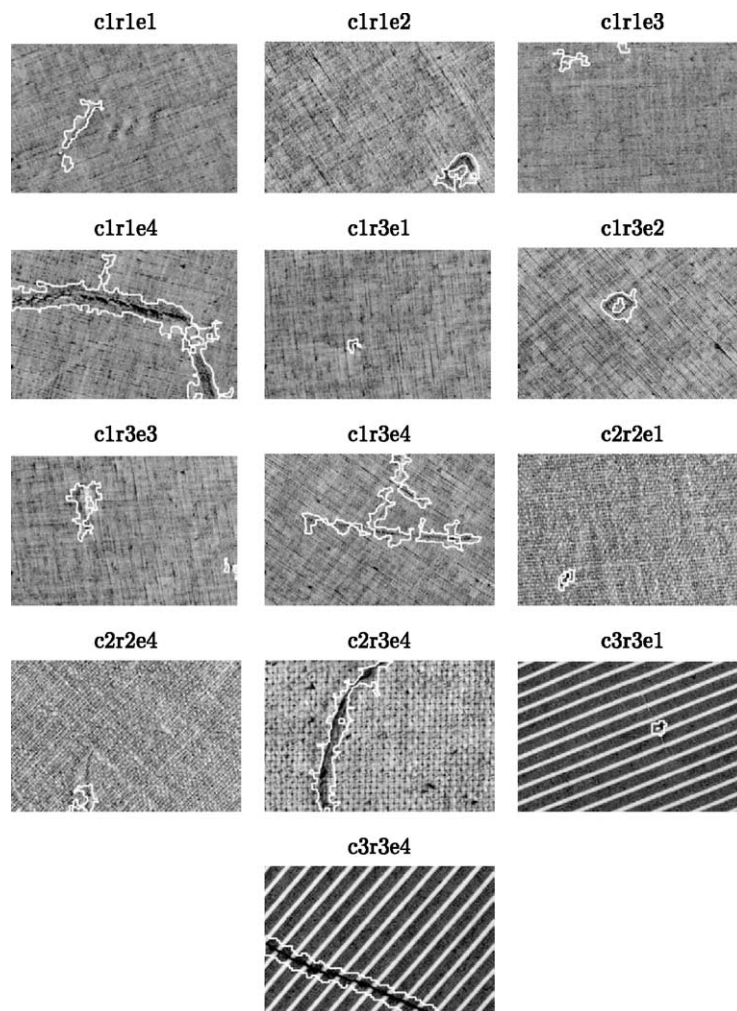


Fig. 11. Test 2. TILDA images. Sample results of the orientation approach. Cases when detection is possible.

occupy a small portion of the window. The window must be relatively large to include at least two periods of the structure.

The orientation approach is more local, and it does not assume periodicity. This approach is obviously not applicable to isotropic patterns. It is most appropriate for unidirectional, flow-like textures, either periodic or not. The orientation method has also been applied to multidirectional patterns in this paper. These patterns often still exhibit an overall dominant orientation, which is evidently less marked than for unidirectional patterns.

A perturbation in the orientation or orientation coherence fields does not necessarily imply a defect, as some non-defect regions often produce the same effect. A solution to this is to expand the description of the defect to include complementary visual cues such as intensity features or size, taking these into consideration using mathematical morphol-

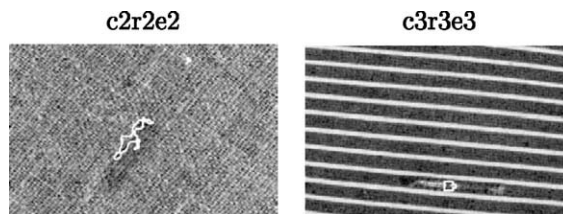


Fig. 12. Test 2. TILDA images. Sample results of the orientation approach. Uncertain cases.

ogy. From a theoretical point of view, this is a drawback, as the orientation approach is not based on a single visual concept. However, the extra features used are physically intuitive. In addition, the incorporation of appearance features may be advantageous from practical point of view, as it

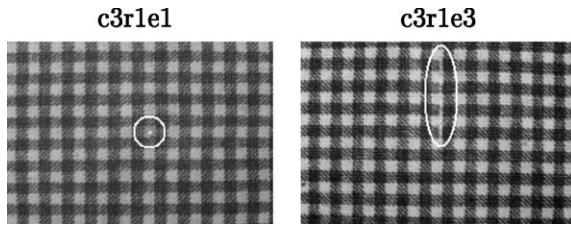


Fig. 13. Test 2. TILDA images. Defects that cannot be detected by either of the two approaches. The defective regions are emphasised.

allows more flexibility when tuning the algorithm to specific defects.

In conclusion, the approaches presented in this paper support and complement each other in a natural and understandable way, providing a framework for future research on texture defect detection.

### Acknowledgements

Dmitry Chetverikov was supported by the Hungarian Scientific Research Fund under grants OTKA T026592 and M28078. Allan Hanbury was supported by a travel grant from the Centre National des Œuvres Universitaires et Scolaires (CNOUS), France.

### References

- [1] T.S. Newman, A.K. Jain, A survey of automated visual inspection, *Comput. Vision Image Understanding* 67 (1995) 231–262.
- [2] S. Özdemir, A. Baykut, R. Meylani, A. Erçil, A. Ertüzün, Comparative evaluation of texture analysis algorithms for defect inspection of textile products, in: *Proceedings of the International Conference on Pattern Recognition*, Brisbane, Australia, Vol. 2, 1998, pp. 1738–1741.
- [3] M. Schael, H. Burkhardt, Automatic detection of errors in textures using invariant grey scale features and polynomial classifiers, in: M.K. Pietikäinen (Ed.), *Texture Analysis in Machine Vision*, Vol. 40, World Scientific, Singapore, 2000, pp. 219–229.
- [4] C.W. Kim, A.J. Koivo, Hierarchical classification of surface defects on dusty wood boards, *Pattern Recognition Lett.* 15 (1994) 713–721.
- [5] J. Iivarinen, A. Visa, An adaptive texture and shape based defect classification, in: *Proceedings of the International Conference on Pattern Recognition*, Brisbane, Australia, Vol. 1, 1998, pp. 117–123.
- [6] A. Serafim, Segmentation of natural images based on multiresolution pyramids linking: application to leather defects detection, in: *Proceedings of the International Conference on Pattern Recognition*, 1992, pp. 41–44.
- [7] D. Chetverikov, Texture imperfections, *Pattern Recognition* 6 (1987) 45–50.
- [8] D. Chetverikov, K. Gede, Textures and structural defects, in: G. Sommer, K. Daniilidis, J. Pauli (Eds.), *Lecture Notes in Computer Science*, Vol. 1296, Springer, Berlin, 1997, pp. 167–174.
- [9] K.Y. Song, M. Petrou, J. Kittler, Wigner based crack detection in texture images, in: *Fourth IEEE International Conference on Image Processing and its Applications*, 1992, pp. 315–318.
- [10] K.Y. Song, J. Kittler, M. Petrou, Defect detection in random colour textures, *Image Vision Computing* 14 (1996) 667–683.
- [11] K.Y. Song, M. Petrou, J. Kittler, Texture defect detection: a review, in: *SPIE Applications of Artificial Intelligence X: Machine Vision and Robotics*, Vol. 1708, SPIE, 1992, pp. 99–106.
- [12] J.M.H. Du Buf, M. Kardan, M. Spann, Texture feature performance for image segmentation, *Pattern Recognition* 23 (1990) 291–309.
- [13] D. Chetverikov, Fundamental structural features in the visual world, in: *Fundamental Structural Properties in Image and Pattern Analysis*, Vol. 130, Österreichischen Computer Gesellschaft, 1999, pp. 47–58.
- [14] A.R. Rao, G.L. Lohse, Identifying high level features of texture perception, *CVGIP: Image Process.* 55 (1993) 218–233.
- [15] R. von der Heydt, E. Peterhans, M.R. Dürsteler, Periodic-pattern-selective cells in monkey visual cortex, *J. Neurosci.* 12 (1992) 1416–1434.
- [16] P. Kruizinga, N. Petkov, Nonlinear operator for oriented texture, *IEEE Trans. Image Process.* 8 (1999) 1395–1407.
- [17] A.R. Rao, A Taxonomy for Texture Description and Identification, Springer, Berlin, 1990.
- [18] J. Bigün, G.H. Granlund, J. Wiklund, Multidimensional orientation estimation with applications to texture analysis and optical flow, *IEEE Trans. Pattern Anal. Mach. Intell.* 13 (1991) 775–790.
- [19] D. Chetverikov, Pattern regularity as a visual key, *Image Vision Computing* 18 (2000) 975–985.
- [20] I. Pitas, *Digital Image Processing Algorithms*, Prentice-Hall, Englewood Cliffs, NJ, 1993.
- [21] P.J. Rousseeuw, A.M. Leroy, *Robust Regression and Outlier Detection*, Wiley Series in Probability and Mathematical Statistics, Wiley, New York, 1987.
- [22] J. Serra, *Image Analysis and Mathematical Morphology*, Academic Press, London, 1982.
- [23] P. Soille, *Morphological Image Analysis: Principles and Applications*, Springer, Berlin, 1999.
- [24] P. Brodatz, *Textures: A Photographic Album for Artists and Designers*, Dover, New York, 1966.
- [25] Workgroup on Texture Analysis of DFG, TILDA textile texture database. <http://lmb.informatik.uni-freiburg.de/research/dfg-texture/tilda>.
- [26] R.A. Peters II, Mathematical morphology for angle-valued images, in: *Non-Linear Image Processing VIII. SPIE*, Vol. 3026, 1997.
- [27] N.I. Fisher, *Statistical Analysis of Circular Data*, Cambridge University Press, Cambridge, 1993.
- [28] G. Mamic, M. Bennamoun, Automatic flaw detection in textiles using a Neyman–Pearson detector, in: *Proceedings of the International Conference on Pattern Recognition*, Barcelona, Spain, Vol. 4, 2000, pp. 767–770.
- [29] A. Bodnarova, M. Bennamoun, S.J. Latham, Textiles flaw detection using optimal Gabor filter, in: *Proceedings of the International Conference on Pattern Recognition*, Barcelona, Spain, Vol. 4, 2000, pp. 799–802.

**About the Author**—DMITRY CHETVERIKOV received his MS degree in Theoretical Physics from the Moscow State University, Russia, in 1978. He received his Ph.D. degree in computer science from the Hungarian Academy of Sciences in 1988. Currently, he is Senior Research Fellow at the Computer and Automation Research Institute and Associate Professor at the Eotvos Lorand University in Budapest, Hungary. Chetverikov is author or co-author of about 100 papers in Computer Vision, Image Processing and Pattern Recognition. For over 10 years he was a member of the Governing Board of the International Association for Pattern Recognition (IAPR). He is on the Editorial Boards of Machine Graphics and Vision and International Journal on Pattern Recognition and Artificial Intelligence. His research interests include texture, motion and shape analysis, scene reconstruction from multiple views, and industrial applications.

**About the Author**—ALLAN HANBURY was born in George, South Africa, in March 1974. He received the B.Sc. (Hons.) and M.Sc. degrees in Physics from the University of Cape Town, South Africa, in 1995 and 1999, respectively. He is presently a researcher at the Centre of Mathematical Morphology, Paris School of Mines, France, where he is working towards the Ph.D. degree. His main topics of research are the application of mathematical morphology to images encoding directional information, defect detection in textures, and the development of algorithms for real-time wood inspection applications.